

ELASTICITY IMAGING

MICHAEL F. INSANA
University of Illinois at Urbana-
Champaign
Urbana, Illinois

1. INTRODUCTION

Elasticity imaging refers to a broad range of imaging and signal processing techniques for the purpose of displaying mechanical properties of tissue (1,2). A common feature of each technique is the application of a mechanical force stimulus and the use of a medical imaging device to track the resulting tissue deformation. The applied forces can be naturally occurring, e.g., pulsatile blood flow, or externally applied. The role of the imaging device is to provide a time series of images (or pre-image data) that track the movements of tissue microstructures. Time series data are combined to map the spatial and temporal distributions of the deformation. Material properties of tissue are found from relationships between forces and deformations. Phase-sensitive imaging modalities—ultrasound, magnetic resonance (MR), and optical—are most sensitive to motion; they can track submicron-scale displacements with sub-millimeter-scale spatial resolution. A simple view of elasticity imaging is tissue palpation by remote sensing.

Physicians have known for thousands of years that tissues frequently stiffen as diseases appear and progress, e.g., liver cirrhosis, myocardial infarction, inflammation, atherosclerotic plaques, and cancer. Consequently, manual palpation will always be part of the physical examination. When a cancerous tumor forms, for example, edema (excessive intracellular fluid) accumulates from early inflammatory responses and as lymphatic drainage is lost with increasing hyperplasia (abnormal cell density and structure). In addition, collagen production is upregulated as mutated epithelial cells signal the surrounding connective tissues to prepare for neo-angiogenesis (new growth of blood vessels). Edema, hyperplasia, and desmoplasia (active fibrotic formation) can stiffen the affected tissues 50 times more than the surrounding regions (3) often before other symptoms appear. Compared with x-ray imaging, tissue stiffness provides much higher object contrast for diagnosis.

Manual palpation is such a simple procedure that it is recommended that women examine themselves routinely for the first signs of breast cancer. Currently most cancers found in patients younger than 45 years, a group that is traditionally one of the hardest to diagnose, is through breast self-examinations (4). During lumpectomies, surgeons will feel the tissues surrounding the surgical site to search for smaller undetected lesions in the area. Lesions that vary only in stiffness are undetected by traditional imaging methods because imaging is generally insensitive to mechanical stiffness unless elasticity imaging techniques are first applied to the signals. Researchers studying elasticity imaging methods are hoping to tap into a vast underdeveloped potential of mechanical properties for diagnosis.

This article reviews basic approaches to elasticity imaging. An exhaustive list could be categorized based on the imaging modality employed, the mechanical property that is mapped into the image, the type of mechanical stimulus applied, or the organ system and disease process under investigation. Despite its brief two-decade history, a concise and comprehensive review would be difficult to complete and is perhaps premature. So we concentrate on our experience applying ultrasonic strain imaging of quasi-static external deformations for breast cancer detection. The next section begins with a specific example and finishes with a brief overview of the broader literature. Later sections describe the physics of tissue deformation and the fundamentals of static ultrasonic elasticity image reconstruction. The breadth of approaches to elasticity imaging is an indication of the broad range of opportunities for new insights into biological mechanisms and medical diagnosis.

2. BACKGROUND

The physical principles of manual palpation (Fig. 1) are reviewed to compare and contrast with those of static ultrasonic elasticity imaging (Fig. 2). First, we define some terminology. Stress is the force per area ($1 \text{ Pa} = 1 \text{ N/m}^2$); it can be positive (compression) or negative (tension). Strain is a unitless quantity of deformation; it is defined as the relative change in length and is positive under compression and negative under tension (although the sign convention is arbitrary). Stresses and strains are properties of the tissue and the experiment. Elastic moduli (there are many) strive to describe material properties independent of the experiment. Young's modulus E , for example, is the ratio of uniaxial stress to corresponding uniaxial strain. It has the units of stress. From the definition, materials with

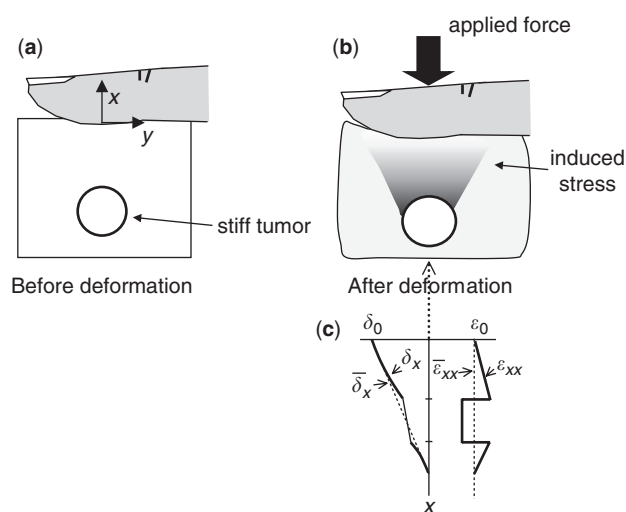


Figure 1. Manual palpation of a stiff circular inclusion is illustrated. Part (c) is a diagram of the displacement δ and strain ϵ profiles as a function of depth along the x -axis through the center of the inclusion.

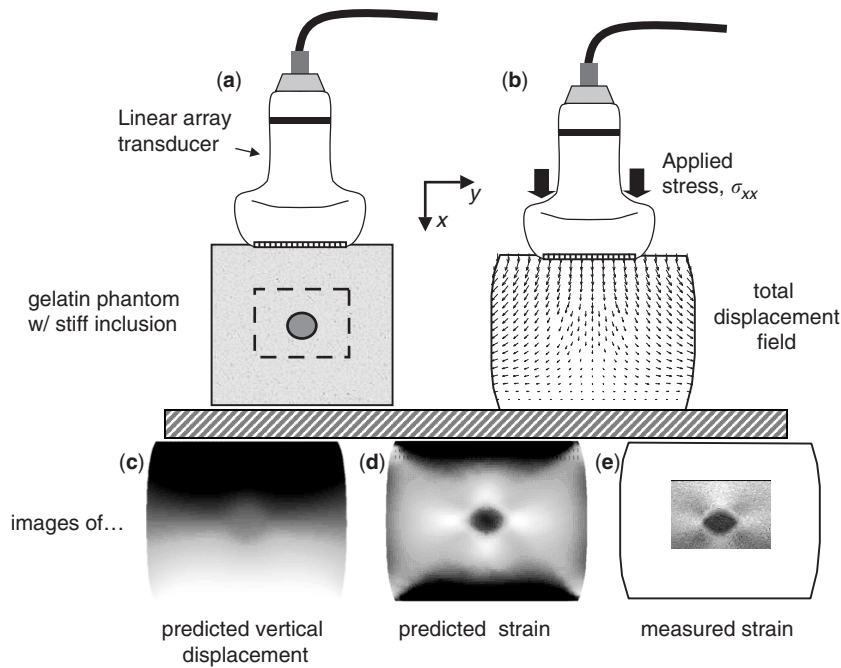


Figure 2. Illustration of an ultrasonic elasticity imaging experiment for the situation in Fig. 1. Downward compression of the top surface in (a) generates the displacement field in (b). Images (c)–(e) are examples of predicted and measured displacements and strains.

large E values deform relatively little when subjected to large compressive or tensile forces—they are stiff.

2.1. Palpation and Static Strain Imaging Examples

Lesions are palpated by gently pressing fingertips into the skin surface to deform the tissues below (Fig. 1a). Because tissues are elastic, a restoring force develops that pushes back against the fingers roughly in proportion to the deformation applied. This is Hooke's law for elastic media, which states that the stress σ and strain ε are linearly related through Young's modulus (5)

$$\sigma = E\varepsilon. \quad (1)$$

As we will see, Equation 1 is a gross simplification of the more complicated analysis required to accurately describe this seemingly simple deformation experiment. Yet the complexity is a rich source of information about tissues.

The induced stress at the skin surface is sensed by the fingertips (Fig. 1b).¹ Stiff regions that lie below the fingers will deform very little, so the surface stress increases as the tissues above and below the stiffness compensate by deforming more. Unfortunately the magnitude of the stress decays quickly with depth, so superficial lesions are more readily detected with palpation. Also palpation provides no depth resolution for locating the position of lesions.

Elasticity imaging can improve on manual palpation by combining the naturally high contrast for stiffness provided by the body with the high sensitivity, depth of pene-

tration, and spatial resolution for motion detection provided by imaging modalities. Figure 2a illustrates a simple ultrasound phantom elasticity experiment analogous to the example in Fig. 1. An 8-mm-diameter circular inclusion is embedded in a uniform gelatin block. Although it has about twice the stiffness of the tissue-like gelatin, the inclusion cannot be palpated from the top surface. A linear array transducer is positioned at the top to record an ultrasound frame of echo data. The transducer is pressed into the top surface a distance of about 1–2% of the total height of the block with the bottom surface held fixed and the sides free to move, and then a second echo frame is recorded. We track the movement of echoes to measure the displacement field. Of course, the gelatin block moves in three dimensions, so we try to control object boundaries to keep as much of the motion as possible in the imaging plane.

If successful, then the movement of ultrasonic echoes can faithfully represent that of the tissue scatterers. The displacements depicted by arrows in Fig. 2b were found using finite element simulation software on a coarse grid. The vertical component of displacement, which is also along the axis of the ultrasound beam, is obtained from a finely sampled grid and converted into grayscale to give the vertical (axial) displacement image in Fig. 2c. The derivative of displacement gives the strain image in Fig. 2d. Strain is preferred over displacement for imaging because of higher image contrast (compare Fig. 2c and Fig. 2d). We built this phantom and performed the imaging experiment described over a subregion surrounding the stiff inclusion (6). The result is shown in Fig. 2e.

The central dark region in strain indicates a region of low deformation and high stiffness. However, regions at the top and bottom appear dark because we did not let those surfaces slip during compression to show the effects of boundaries. In clinical imaging, the skin surface is often

¹Fingers sense stress more acutely than net force. For example, a sharpened pencil pressed into your fingertip with a force of 1 N will raise your attention much faster than an unsharpened pencil at a force of 10 N because the smaller area contacting the skin generates high surface stress.

lubricated to allow the transducer to slip over the surface during compression. Strain images can be interpreted as the inverse of Young's modulus (stiffness) via Equation 1, only when the applied stress is constant throughout, which it was not in Fig. 2.

Figure 1c illustrates how displacement $\delta_x(x)$ and strain $\varepsilon_{xx}(x)$ develop along the x axis (the notation is described below). The surface near the fingertips is displaced downward by the amount δ_0 . If the stiffness of the elastic tissue were constant, we would observe a linear displacement curve (dotted line) and the associated strain, given by the derivative $\varepsilon_{xx}(x) = d\delta_x/dx$, would be constant ε_0 . However, this medium is heterogeneous. Because stiff objects deform less than their surroundings, regions above and below deform more to keep the total deformation at δ_0 . Taking the derivative, we find lower strain in the inclusion and enhanced strain immediately surrounding the inclusion. Contrast enhancement is also seen in the modeled and measured strain images of Fig. 2 as a bright region surrounding the stiff inclusion.

3. CHOOSING FORCE STIMULUS AND IMAGING MODALITY

The nature of the stimulating mechanical force determines which mechanical and geometrical properties of the tissue contribute to image contrast. Stimuli may be generalized as static (the example above) or dynamic. *Static methods* employ forces that are suddenly applied and held constant during imaging or allowed to slowly vary in time with respect to the temporal sampling of the imaging system, e.g., the frame rate. We imaged strain in the example above; however, strain may also be combined with stress estimates through constitutive equations (5) to display a modulus (7) and thereby minimize boundary effects. The advantages of modulus imaging must be compared with the extra computation time and any change in image quality or interpretation that affects diagnosis.

The first studies to include elasticity imaging involved measurements of deformations from slowly moving endogenous sources, like pulsatile blood flow (8,9). Later methods measured deformations from exogenous sources such as compression plates for *in vivo* breast imaging (10) and balloons for *in vivo* vascular (11) and prostate (12) imaging. These methods are examples of static (or sometimes quasi-static) elasticity imaging. The principal limitation of static strain imaging is the strong influence of boundaries on image contrast (e.g., Fig. 2d). Advantages include the use of current image systems and the simplicity of the calculation that allows high frame rates (commensurate with color-flow imaging) with spatial resolution approaching the intrinsic resolution of the host imaging modality.

In *dynamic methods*, tissues are stimulated with low-frequency (100 Hz) shear-wave vibrations. As surface vibrations travel into the body, ultrasound pulses are introduced and echoes are recorded. The first methods measured the amplitude (13) and phase (14) of the low-frequency vibrations from the Doppler modulation frequency of the ultrasound pulses to estimate viscoelastic parameters of muscle and other soft tissues. The approach

became more practical for clinical investigations of tumor imaging when color-Doppler systems were adapted to image vibrations (15). Shear waves are attenuated in tissues much more than compressional waves (ultrasound pulses), so it can be difficult to mechanically stimulate tissues deep in the body. Continuous-wave (CW) shear vibrations allow repeated measurements and temporal averaging when the imaging signals are weak; yet some of the CW vibrational energy can be reflected from boundaries and form standing waves that interfere with image clarity.

Magnetic resonance elastography (MRE) can provide distinct advantages over current ultrasonic imaging techniques (16). As in dynamic ultrasound approaches, an applicator is coupled to the skin surface to introduce low-frequency shear waves into the body. MR signals are used to measure displacement distributions from traveling shear waves in the tissue volume. Displacement waves describe the wave speed from which shear modulus images are quickly computed. (For example, see text below Equation 10.) MR methods have also been proposed to image strain from static deformations (17). The principal advantage over ultrasound is that MR provides finely sampled image data from a tissue volume. Volume acquisition reduces signal loss from tissues moving out of the field, and it allows for a more complete estimation of the strain tensor (18). Current disadvantages (compared with ultrasound) include lower temporal resolution and higher imaging costs. The future commercialization of two-dimensional ultrasound arrays suggests the acquisition of volumetric ultrasound data may not be far away. Also, phase array MR techniques are promising to improve MR temporal resolution. So the advantages and disadvantages of each modality vary as technology develops.

Very high frame rate ultrasound techniques (> 1000 f/s) have been shown capable of imaging shear wave propagation in real time (19). The advantage of this approach is the possibility of using shear-wave pulses that locally stimulate tissues. Localization of the stimulus eliminates boundary effects and makes it possible to separate the influence of material elastic anisotropy from object shape, thus increasing the feature space for diagnosis. Acoustic radiation force impulse (ARFI) methods (20,21) use the radiation force generated by a high-intensity compressional wave pulse at its focus to stimulate tissues with a force "impulse" in both time and space. Then conventional broadband imaging pulses scan the medium to record the movement. Like static methods for mechanical stimulation, the elastic modulus of the medium contributes to the object contrast. Unlike static methods, viscous effects also play a major role in contrast, and the isolated "push" from the radiation force of the high-intensity pulse reduces boundary effects significantly. The downside of very high frame rate and ARFI approaches is that specialized equipment is needed, and in the ARFI approach, the use of high intensity pulses raises concerns about risks to the transducer and patient.

Vibro-acoustic imaging (22) is another promising approach, particularly for locating calcified tissues in vascular plaques and tumors. Two co-axial CW ultrasound beams tuned to slightly different transmission frequencies generate a harmonic radiation force that oscillates

tissue at the difference frequency near the focus. If stiff tissues, like calcifications, are in the stimulated region, they radiate sound energy at the difference frequency, which is in the audible frequency range. Spatial resolution depends on the co-axial pulse volume stimulating the tissue, and image contrast depends on the mechanical properties of the tissue. Sensitivity and noise are affected by the ability of audible sound to travel out of the body to be detected by a microphone with a high signal to ambient noise ratio. Because low-intensity beams stimulate the tissues, bioeffects are not a major concern. However, it is challenging to design transducers that deliver a highly local radiation force that can be scanned electronically at real-time frame rates.

There are many other exciting and promising approaches. For example, MR spin tagging methods are applied to evaluate the dynamics of the heart motion (23), and ultrasonic strain rate imaging (sometimes called tissue Doppler imaging) has been used for functional myocardial assessment (24). Optical coherence tomography can be applied like ultrasound to image displacement and strain in atherosclerotic tissues but with much greater motion sensitivity and spatial resolution (25). Others have used optical tweezers to stress individual DNA (deoxyribo nucleic acid) molecules and optical microscopy to image the displacement (26). The goal was to discover how molecular stiffness affects transcription and replication. An excellent source of information about many elasticity imaging approaches can be found in a special issue in *Physics in Medicine and Biology*, vol. 45, June 2000. It offers 300 pages of detailed descriptions. Recent reviews of the physics (1) and engineering (2) of elasticity imaging are also available.

AU:1

4. FUNDAMENTAL EQUATIONS

Other aspects shared by all elasticity imaging methods are the basic equations that describe (1) the displacement of tissues by a mechanical stimulus and (2) the constitutive equations that relate stress to strain. The underlying assumptions are that tissues are a deformable continuum² and that local displacements are small; e.g., $(\partial\delta_x/\partial x)^n$ is negligible for $n > 1$. The last assumption may seem difficult to achieve considering that strain contrast increases with the amount of applied deformation. However, if the image data are acquired at a high frame rate while the forces are applied, the instantaneous displacements between frames can be accumulated (27), thus satisfying the assumption for estimation purposes while still enhancing image contrast.

²Tissues are a volume of interconnected particles. Define a surface area element ΔS somewhere in the volume where ΔF is the force due to particles on one side of the surface that act on particles located on the other side. If the medium has mass density ρ and stress σ that can be defined as $\sigma = \lim_{\Delta S \rightarrow \text{small}} \Delta F/\Delta S$, then the medium is a material continuum (5).

4.1. Constitutive Equations

To design elasticity imaging experiments and correctly interpret the results, it is critically important to understand how the stress loading of tissues and the measurement of displacement or strain determine which material properties influence the elasticity image. Equation 1 is a very simple constitutive equation that applies to infinitesimal deformations of one-dimensional, elastic, isotropic media where the strains vary linearly with stress. Although none of these assumptions are strictly true in practice (5), they may be reasonable to assume for some experimental conditions.

Let's extend the medium to three dimensions leaving other assumptions in place. To do this we must recognize that the elements of Equation 1 are tensors, and the general linear relation is (28)

$$\sigma_{ij} = C_{ijkl}\varepsilon_{kl}. \quad (2)$$

The stress σ and strain ε tensors are second order (3×3 matrices) and symmetric if we avoid translation and rotation of the tissues from the applied forces. Indices $ijkl$ are variables for the coordinate labels (xyz). For example, σ_{xy} refers to the stress on a Cartesian surface with unit normal given by the x -axis where the force is oriented along the y -axis, i.e., a shear stress. Cauchy's infinitesimal strain tensors (5) are found from derivatives of the displacement vector, $\varepsilon_{xy} = \frac{1}{2}\left(\frac{\partial\delta_y}{\partial x} + \frac{\partial\delta_x}{\partial y}\right)$. The fourth-order modulus tensor C contains elastic material constants that characterize the medium. As σ and ε are symmetric, it can be shown that C has at most 21 unique components even if the medium is fully anisotropic. Using directional cosines to define the isotropic axes of symmetry for all three tensors in Equation 2, we find there are only two unique terms: $C_{xxxx} = \lambda + 2G$ and $C_{xxyy} = \lambda$, where λ and G are Lamé constants described below. (Interested readers are referred to Chapter 1 of Ref. 28 for detailed derivations of modulus tensors given various material property symmetries.)

The three-dimensional version of Hooke's law in Equation 2 simplifies for isotropic media:

$$\sigma_{ij} = \lambda \text{tr}(\varepsilon)\delta_{ij} + 2G\varepsilon_{ij}, \quad (3)$$

where $\text{tr}(\varepsilon) = \varepsilon_{xx} + \varepsilon_{yy} + \varepsilon_{zz}$ is the trace of the strain matrix that quantifies how much the *volume* of the medium changes due to the applied stress and δ_{ij} is the Kronecker delta. Equation 3 is Navier's equation for an isotropic Hookean elastic solid (29). Strain may be separated into two parts, $\varepsilon_{ij} = \varepsilon'_{ij} + \varepsilon''_{ij}$, where $\varepsilon'_{ij} = \frac{1}{3}\text{tr}(\varepsilon)\delta_{ij}$ is the mean dilation or contraction of the volume and ε''_{ij} the deviation of the deformation about the mean value. This decomposition allows the diagonal stresses of Equation 3 to be written as

$$\sigma_{ij} = 3K\varepsilon'_{ij} + 2G\varepsilon''_{ij}, \quad \text{for } i=j, \quad (4)$$

where $K = \lambda + 2G/3$. K is the *bulk modulus* that describes how the medium *volume* changes under stress. G is the *shear modulus* that quantifies how the medium *shape*

changes under the same stress. K and G are fundamental properties of the medium, although the convenient separation of strain into volumetric and shape components in Equation 4 is only valid for infinitesimal deformations. The numerical constants in Equations 3 and 4 develop because of traditional definitions relating the bulk modulus to isotropic pressure, $p = -K \text{tr}(\varepsilon)$, and the shear modulus to the amount of shear deformation $\gamma = 2\varepsilon_{xy}$, viz., $\sigma_{xy} = G\gamma$.

It is often more convenient to propose *derived moduli* for the experimental geometry that are combinations of *fundamental moduli*. With all of the elastic moduli in the literature, it can be confusing to tell which are fundamental and derived. To illustrate a common derived modulus, we return to the static strain experiment of Fig. 2 where a compressional stress is applied to the top surface of a gelatin phantom along the x -axis, i.e., σ_{xx} . The stress and strain matrices for this experiment are

$$\sigma = \begin{bmatrix} \sigma_{xx} & 0 & 0 \\ 0 & 0 & 0 \\ 0 & 0 & 0 \end{bmatrix} \quad \text{and} \quad \varepsilon = \begin{bmatrix} \varepsilon_{xx} & 0 & 0 \\ 0 & \varepsilon_{yy} & 0 \\ 0 & 0 & \varepsilon_{yy} \end{bmatrix}. \quad (5)$$

Notice that strain components in the yz -plane are equal. The convenient derived quantities are Young's modulus, $E = \sigma_{xx}/\varepsilon_{xx}$ and Poisson's ratio $\mu = -\varepsilon_{yy}/\varepsilon_{xx}$. Isotropic media have two independent fundamental moduli, and so two derived quantities are needed to characterize the medium for this experiment. Substituting Equation 5 into Equation 3,

$$\begin{aligned} \sigma_{xx} &= \lambda(\varepsilon_{xx} + 2\varepsilon_{yy}) + 2G\varepsilon_{xx} \\ 0 &= \lambda(\varepsilon_{xx} + 2\varepsilon_{yy}) + 2G\varepsilon_{yy}. \end{aligned} \quad (6)$$

Solving for σ_{xx} and ε_{xx} , we can relate Young's modulus and Poisson's ratio to the fundamental moduli $E = \frac{9KG}{3K+G}$ and $\mu = \frac{3K-2G}{6K+2G}$. It turns out that the bulk modulus is orders of magnitude larger than the shear modulus in biological tissues, $K \gg G$, so we can approximate $E \cong 3G$ and $\mu \cong 0.5$. Tissues are said to be "nearly incompressible," meaning the volume change when you squeeze them is not measurable. Lower G values mean that tissues do change shape. Now we know that the strain images in Fig. 2 reflect shape deformations caused by spatial variations in shear modulus (and, unfortunately, boundary effects).

The effects of boundaries are very important for static deformations because they modify Equation 5. The fact that we did not let the top and bottom surfaces in Fig. 2b slide during compression or restrict movement of the lateral boundaries had major influences on the stresses and strains near the periphery. If we could measure the full stress and strain tensors for each location, we could propose convenient derived quantities for imaging that could be directly related to K and G . Insofar as tissues are incompressible and isotropic, ε_{xx} measurements may be used to infer the value of other strain components via μ , but tell us nothing about stress. As described, the strength of MRE is its ability to measure displacements in three di-

mensions (17), so at least the full strain tensor can be measured.

Material properties that affect compressional (ultrasonic imaging) wave propagation can also be identified with these equations. As compressional³ plane waves propagate along the x -axis, tissues compress and stretch in high- and low-pressure regions along the x -axis. The stress and strain matrices for these conditions are

$$\sigma = \begin{bmatrix} \sigma_{xx} & 0 & 0 \\ 0 & \sigma_{yy} & 0 \\ 0 & 0 & \sigma_{yy} \end{bmatrix} \quad \text{and} \quad \varepsilon = \begin{bmatrix} \varepsilon_{xx} & 0 & 0 \\ 0 & 0 & 0 \\ 0 & 0 & 0 \end{bmatrix}. \quad (7)$$

Derived quantities for this experiment are the wave modulus $M = \sigma_{xx}/\varepsilon_{xx} = K + 4G/3$ and stress ratio $\sigma_{yy}/\sigma_{xx} = (K - 2G/3)/(K + 4G/3)$ (28). Because $K \gg G$, $M \cong K$, and the stress is isotropic, $\sigma_{yy}/\sigma_{xx} \cong 1$, which is an important result for ultrasound-based elasticity imaging. It tells us that sound propagation and tissue deformation depend on different material properties of the tissue. Although sound propagation depends on the bulk modulus, deformations depend on the shear modulus. If they were not independent, then deformations would alter the echo signals and ultrasound would not be able to accurately track tissue motion.

4.2. Equations of Motion

Equation 3 is often the launching point for the development of elasticity imaging. For linear, elastic, isotropic solids, K , G , and mass density ρ completely characterize the mechanical properties. In regions where these values are spatially homogeneous and the effects of gravity can be ignored, the displacement vector δ may be expressed as (1,2)

$$G\nabla^2\delta + \left(K + \frac{G}{3}\right)\nabla(\nabla \cdot \delta) = \rho \frac{\partial^2\delta}{\partial t^2}. \quad (8)$$

The dynamic response of the medium to the various mechanical stress and strain stimuli described in previous sections can be found by considering the special cases of Equation 8.

4.3. Compressional Wave Propagation

As we saw in the previous section, local pressures in compressional waves are given by a symmetric stress tensor. Consequently, the curl of the displacement vector, $\nabla \times \delta$, is zero (30) so that $\nabla^2\delta = \nabla(\nabla \cdot \delta)$. Substituting this identity

³Particle motion is parallel to wave motion for compressional waves. Particle motion is perpendicular to wave motion for shear waves.

6 ELASTICITY IMAGING

into Equation 8

$$\left(K + \frac{4G}{3}\right) \nabla(\nabla \cdot \delta) = \rho \frac{\partial^2 \delta}{\partial t^2} \quad (9)$$

$$\nabla^2 \delta = \frac{1}{c^2} \frac{\partial^2 \delta}{\partial t^2},$$

where $c = ((K + 4G/3)/\rho)^{1/2}$ is the speed of a compressional displacement wave. The response of the medium to a stimulus may also be written as density waves but most often appears in the literature as pressure waves (30).

4.4. Shear Wave Propagation

Shear waves are central to dynamic elasticity imaging methods. They produce no dilation or contraction of the medium, so the divergence of displacement, $\nabla \cdot \delta$, is zero and Equation 8 reduces to

$$\nabla^2 \delta = \frac{1}{c_s^2} \frac{\partial^2 \delta}{\partial t^2}, \quad (10)$$

where $c_s = (G/\rho)^{1/2}$ is the speed of the shear wave. Again we notice that $K \gg G$ so that $c \gg c_s$. The large speed difference allows use of ultrasonic imaging to observe traveling shear waves in dynamic elasticity imaging (19–21).

4.5. Step Compression

If we apply and hold a step compression, then in steady state, the time derivatives and divergence of displacement are both zero. Equation 8 reduces simply to Laplace's equation (1), $\nabla^2 \delta = 0$. This tells us that displacements in homogeneous media are linear functions of position, of the form $\delta_x(x) = \epsilon_0 x + \delta_0$ in one dimension (see Fig. 1c), and thus strains are constant. If we examine Fig. 2d, we see that compressed heterogeneous media do not give even piece-wise linear displacements or constant regional strains regardless of the boundary effects. The dark (stiff) region in the center of the strain image is surrounded by a bright enhancement. When material properties ρ , K , G vary spatially, Equation 8 must be generalized to more accurately predict displacement and strain patterns. Specifically, terms are added to Equation 8 that account for the heterogeneities. Closed-form expressions to more accurately predict the situations depicted in Figs. 1c and 2d are available (31).

5. IMAGE FORMATION

The previous section outlined the physics of elastic deformation to help readers understand the advantages and limitations of different approaches to elasticity imaging. This section discusses the basics of image formation specifically for static ultrasonic strain imaging. Reconstruction of elasticity images from dynamic stimuli and modulus images from static stimuli is discussed elsewhere (2,7,18).

Imaging strategies are based on models of signal formation, which requires an understanding of how tissue

properties create the imaging signals (see ultrasonic imaging) and how stress stimuli deform the tissue properties (previous section). Common features of imaging algorithms are described below.

5.1. Modeling Object Structures and Their Echo Signals (32)

Let $f_j(x)$ be the scattering function that describes the spatial distribution of structures interacting with an ultrasound pulse to produce detectable scattered waves during acquisition of the j th ultrasonic echo frame. This is a natural representation because tissue scattering is a continuous function of three-dimensional position x . For computer modeling purposes, however, it is convenient to sample $f_j(x)$ and rearrange the values into a column vector f_j by lexicographical reordering.

Scatterer movement is observed by examining the same tissue region during two or more instances in time. Object functions present during the sequential acquisition of echo frames are related by displacement vectors $\delta_j(x)$ that describe the movement of scatterers at each location. In the continuous representation, we have $f_{j+1}(x) = f_j(x + \delta_{j+1}(x))$, and in the discrete representation, $f_{j+1} = Q_{j+1} f_j + e_{j+1}^r$, where Q is a square matrix of displacements in the tissue region occurring between frames. The vector e_{j+1}^r represents registration errors caused by sampling the continuous function.

Scanning the object with a linear imaging system represented by the operator matrix H , we acquire the following radio-frequency (RF) echo signals g_j :

$$g_j = H f_j + e_j \quad \text{and} \quad g_{j+1} = H Q_{j+1} f_j + e_{j+1}, \quad (11)$$

where $e_j = H e_j^r + e_j^a$ and e_j^a is a vector of acquisition errors, e.g., quantization and amplifier noises. The imaging system does not depend on when the data are acquired or the amount of deformation and therefore has no subscript. The vectors g are the RF echo signals recorded by the ultrasound scanner, not the B-mode image data. The objective in elasticity imaging is to estimate Q , which contains the spatial distribution of displacements $\delta_{j+1}(x)$; essentially the map of arrows seen in Fig. 2b.

5.2. Estimating Displacements

To estimate Q , we seek a transformation of g_j , given by the operator matrix D , that makes the following statement true:

$$\begin{aligned} g_{j+1} &= D_{j+1} g_j \\ &= D_{j+1} H f_j + e_j = H Q_{j+1} f_j + e_{j+1}. \end{aligned} \quad (12)$$

The first line tells us to find a matrix D that displaces the echoes of frame j so they match (are highly correlated with) the echoes of frame $j + 1$. The second line tells us this will work perfectly (except for noise) only when the deformation and imaging operators commute; i.e., we can find a matrix $D = Q$ only when $DH = HQ$. Unfortunately this statement is not true in general. To see this, consider that H is a blurring matrix where the rows are impulse

responses (point spread functions) of the imaging system. Deformed tissue structures of size below the spatial resolution of the image system are not faithfully represented in the echo signal, so there is no deformation matrix D that can be applied to the echo signal g_j that allows the right-side equality in the second line of Equation 12 to be true. Equation 12 can be exact (except for noise) only when H equals the identity matrix, i.e., when we use a perfect ultrasonic imaging system where the shift-invariant impulse response is a Dirac delta function. As with all imaging techniques, we are most successful at imaging displacements with the highest resolution imaging systems.

Undeterred by this fundamental limitation, we press on assuming Equation 12 is reasonably accurate. In those situations, displacements are estimated from RF echo frames using constrained optimization; specifically, we seek to define a matrix D' that minimizes the objective function (30)

$$\hat{D}'_{j+1} = \arg \min_{D'} (\|g_{j+1} - D'g_j\|^2 + \alpha \|r\|^2). \quad (13)$$

$\|\cdot\|$ is the norm of the vector, α is a constant, and r is a roughness penalty vector and a function of displacement (33). The approach is simple to explain. Find a displacement matrix D' that minimizes the first terms on the right side of Equation 13 and yet is subject to the constraint that the solution must be spatially smooth, the second term. When you find D' that minimizes this objective function, use it as the estimate \hat{D}' .

The simplest algorithm that follows this strategy is to simply cross correlate subsections of g_j and g_{j+1} to find the average local displacements (6,10,20,21). For small displacements that remain in the scan plane, numerous correlation-based techniques can be unbiased, precise (satisfying the maximum likelihood criterion), and computationally efficient. Interested readers are referred to the general literature on time delay estimation for details on the estimation problem (34). It can be shown that setting α to zero in Equation 13, completing the square, and discarding all but the single remaining cross term is equivalent to finding the displacement that maximizes the cross-correlation function (32). (Terms in g_j^2 and g_{j+1}^2 express the energy of the signals in the two frames. They do not change with deformation provided all motion is in

the scan plane, and therefore they can be discarded without affecting estimates.)

To demonstrate the merits of regularization, i.e., using the smoothness penalty term in Equation 13 by setting $\alpha > 0$, consider the phantom images in Fig. 3. This is a flow phantom that has a stiff, solid central region and a soft flow channel that cuts diagonally across. The 7-MHz B-mode image in Fig. 3a shows both structures as low scattering (hypoechoic). The correlation-based strain image in Fig. 3b from Ref. 6 shows the central region to be stiff (low strain) and the flow channel to be soft (high strain) as expected, although there is plenty of noise particularly near the softer regions than deform to a greater extent. This strain noise is caused by the low RF echo signal-to-noise ratio in the flow channel, by echo decorrelation from motion smaller than the imaging pulse volume, and by some out-of-plane scatterer movement. We increased α in Equation 13 as described in Ref. 33, which constrained the space of possible displacement solutions to those that were spatially smooth. The physics of tissue-like material deformations told us that very rapid oscillations in displacement were nonphysical. The regularization term excludes solutions to the objective function in Equation 13 that are nonphysical. So the fast spatial fluctuations in strain are treated as noise and eliminated. Regularization is dangerous in imaging situations that are not well understood, because prior knowledge is too incomplete to restrict the solution space without incurring bias errors. Regularization compromises the spatial resolution of strain estimates to a degree (notice the flow channel in Fig. 3c is wider than in Fig. 3a or b), but for many situations, the noise improvement makes it worth the effort.

AU:2

6. SUMMARY

The objective of this article is to convince readers that elasticity imaging has much to offer research in biological sciences and medical diagnosis. Although current approaches impose stringent assumptions about the response of tissues to mechanical stimuli and are forced to create images with limited sensory information from the imaging device, they nevertheless provide unique diagnostic information about structure and function. The diversity of approaches to elasticity imaging is testament to the richness and importance of the topic.

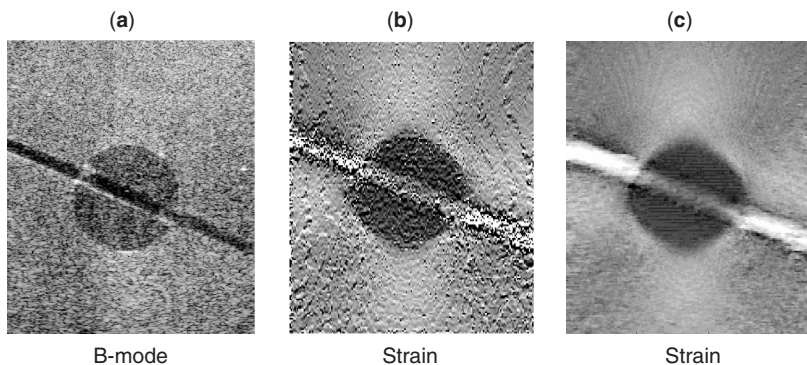


Figure 3. Images of an ultrasonic phantom with a stiff circular inclusion and a soft flow channel. The strain image in (b) was obtained from Equation 12 without regularization, i.e., $\alpha = 0$, using the correlation algorithm described in Ref. 6. The strain image in (c) was also obtained from Equation 12 but with regularization, $\alpha > 0$, and using the optical flow algorithm described in Ref. 33.

Today many researchers apply the methods outlined above to biological tissues in the hope of discovering the range of information available for describing detailed biological processes. Eventually we may find that this simple material science analysis is insufficient; specifically, imaging algorithms will need to be based on more realistic (and complicated) constitutive equations than Equation 3. Modifications might include use of finite stress and strain tensors (29), quasi-linear or nonlinear viscoelastic theory (5), and a fuller accounting of poroelastic and viscoelastic effects (29,36). The natural analytical complexity that adds to the feature space for diagnosis will continue to be exploited as long as there is valuable new information to be obtained.

Acknowledgments

Work from the author's laboratory was supported in part by NIH R01 CA082497 and Siemens Medical Solutions, Mountain View, CA.

BIBLIOGRAPHY

1. K. J. Parker, L. S. Taylor, S. Gracewski, and D. J. Rubens, A unified view of imaging the elastic properties of tissue. *J. Acoust. Soc. Am.* 2005; **117**:2705–2712.
2. J. F. Greenleaf, M. Fatemi, and M. Insana M, Selected methods for imaging elastic properties of biological tissues. *Annu. Rev. Biomed. Eng.* 2003; **5**:57–58.
3. T. A. Krouskop, T. M. Wheeler, F. Kallel, B. S. Garra, and T. Hall, Elastic moduli of breast and prostate tissues under compression. *Ultrasonic Imaging* 1998; **20**:260–274.
4. R. J. Coates, R. J. Uhler, D. J. Brogan, M. D. Gammon, K. E. Malone, C. A. Swanson, E. W. Flagg, and L. A. Brinton, Patterns and predictors of the breast cancer detection methods in women under 45 years of age (United States). *Cancer Causes Contr.* 2001; **12**:431–442.
5. Y. C. Fung, *Biomechanics: Mechanical Properties of Living Tissues*, 2nd ed. New York: Springer-Verlag, 1993.
6. P. Chaturvedi, M. F. Insana, and T. J. Hall, 2-D companding for noise reduction in strain imaging. *IEEE Trans. Ultrason. Ferroelectr. Freq. Contr.* 1998; **UF45**:179–191.
7. F. Kallel and M. Bertrand, Tissue elasticity reconstruction using linear perturbation method. *IEEE Trans. Med. Imaging* 1996; **15**:299–313.
8. R. J. Dickinson and C. R. Hill, Measurement of soft tissue motion using correlation between A-scans. *Ultrasound Med. Biol.* 1982; **8**:263–271.
9. L.S. Wilson and D. E. Robinson, Ultrasonic measurement of small displacements and deformations of tissue, *Ultrason. Imag.* 1982; **4**:71–82.
10. J. Ophir, I. Cespedes, H. Ponnekanto, Y. Yazdi, and X. Li, Elastography: A quantitative method for imaging the elasticity of biological tissues. *Ultrason. Imag.* 1991; **13**:111–134.
11. E.I. Cespedes, C. L. de Korte, A. F. van der Steen, C. von Birgelen, and C. T. Lancee, Intravascular elastography: principles and potentials. *Semin. Interv. Cardiol.* 1997; **2**:55–62.
12. D. L. Cochlin, R. H. Ganatra, and D. F. Griffiths, Elastography in the detection of prostatic cancer. *Clin. Radiol.* 2002; **57**:1014–1020.
13. T. A. Krouskop, D. R. Dougherty, and S. F. Vinson, A pulsed Doppler ultrasonic system for making noninvasive measurements of the mechanical properties of soft tissue. *J. Rehabil. Res. Dev.* 1987; **24**:1–8.
14. Y. Yamakoshi, J. Sato, and T. Sato, Ultrasonic imaging of internal vibrations of soft tissues under forced vibration. *IEEE Trans. Ultrason. Ferroelectr. Freq. Contr.* 1990; **37**:45–53.
15. R. M. Lerner, K. J. Parker, R. Holen, R. Gramiak, and R. C. Waag, Sonoelasticity images derived from ultrasound signals in mechanically vibrated targets. *Ultrasound Med. Biol.* 1990; **16**:231–239.
16. R. Muthupillai, D. J. Lomas, P. J. Rossman, J. F. Greenleaf, A. Manduca, and R. L. Ehman, Magnetic resonance elastography by direct visualization of propagating acoustic strain waves. *Science* 1995; **269**:1854–1857.
17. D. B. Plewes, J. Bishop, A. Samani, and J. Sciarretta, Visualization and quantification of breast cancer biomechanical properties with MRE. *Phys. Med. Biol.* 2000; **45**:1591–1610.
18. R. Sinkus, J. Lorenzen, D. Schrader, M. Lorenzen, M. Dargatz, and D. Holz, High resolution tensor MR elastography for breast tumor detection. *Phys. Med. Biol.* 2000; **45**:1649–1664.
19. L. Sandrin, M. Catheline, M. Tanter, X. Hennegin, and M. Fink, Time-resolved pulsed elastography with ultrafast ultrasonic imaging, *Ultrason. Imag.* 1999; **21**:259–272.
20. W. F. Walker, F. J. Fernandez, and L. A. Negron, A method of imaging viscoelastic parameters with acoustic radiation force. *Phys. Med. Biol.* 2000; **45**:1437–1447.
21. K. R. Nightingale, M. L. Palmeri, R. W. Nightingale, and G. E. Trahey, On the feasibility of remote palpation using acoustic radiation force. *J. Acoust. Soc. Am.* 2001; **110**:625–634.
22. M. Fatemi and J. F. Greenleaf, Ultrasound-stimulated vibroacoustic spectrography. *Science* 1998; **280**:82–85.
23. N. F. Osman and J. L. Prince, Visualizing myocardial function using HARP MRI. *Phys. Med. Biol.* 2000; **45**:1683–1702.
24. Y. Miyasaka, M. Haiden, H. Kamihata, T. Nishiue, and T. Iwasaka, Usefulness of strain rate imaging in detecting ischemic myocardium during dobutamine stress. *Int. J. Cardiol.* 2005; **102**:225–231.
25. J. Rogowska, N. A. Patel, J. G. Fujimoto, and M. E. Brezinski, Optical coherence tomographic elastography technique for measuring deformation and strain of atherosclerotic tissues. *Heart* 2004; **90**:556–562.
26. J. Zlatanova and S. H. Leuba, Stretching and imaging single DNA molecules and chromatin. *J. Muscle Rec. Cell. Motil.* 2002; **23**:377–395.
27. T. Varghese, J. Ophir, and I. Cespedes, Noise reduction in elastograms using temporal stretching with multicompression averaging. *Ultrasound Med. Biol.* 1996; **22**:1043–1052.
28. N. W. Tschoegl, *The Phenomenological Theory of Linear Viscoelastic Behavior*. Berlin: Springer-Verlag, 1989.
29. Y. C. Fung, *Biomechanics: Circulation*, 2nd ed. New York: Springer; 1997.
30. S. Temkin, *Elements of Acoustics*. Melville, NY: AIP Publishing Center; 2001.
31. M. Bilgen and M. F. Insana, Elastostatics of a spherical inclusion in homogeneous biological media. *Phys. Med. Biol.* 1998; **43**:1–20.
32. J. Liu, C. K. Abbey, and M. F. Insana, Linear approach to axial resolution in elasticity imaging. *IEEE Trans. Ultrason. Ferroelectr. Freq. Contr.* 1990; **37**:45–53.
33. C. Pellot-Barakat, F. Frouin, M. F. Insana, and A. Herment, Ultrasound elastography based on multi-scale estimations of displacement regularized fields. *IEEE Trans. Med. Imaging.* 2004; **23**:153–163.

34. G. C. Carter, *Coherence and Time Delay Estimation: An Applied Tutorial for Research, Development, Test, and Evaluation Engineers*. Piscataway NJ: IEEE Press; 1993.
35. L. S. Wilson, D. E. Robinson, and M. J. Dadd, Elastography—the movement begins. *Phys. Med. Biol.* 2000; **45**:1409–1421.
36. P. L. Chandran and V. H. Barocas, Microstructural mechanics of collagen gels in confined compression: Poroelasticity, viscoelasticity, and collapse. *Trans. ASME.* 2004; **126**:152–166.

AU:3

KEYWORDS

cancer, deformation, dynamic imaging, palpation, static, strain, ultrasound

ABSTRACT

Basic principles and examples of elasticity imaging are summarized. The chapter focuses on static ultrasonic methods, and it discusses the advantages and limitations of this approach in the context of dynamic methods and alternative imaging modalities from the literature. We review the physics of continuum deformations as a way to evaluate various experimental approaches. A general strategy for the design of ultrasonic elasticity imaging algorithms for static deformations is also described. The objective is to summarize and critically assess a subset of current approaches to this exciting new field.

Author Query Form



Title: Encyclopedia of Biomedical Engineering
Article/Number: Elasticity Imaging/jwus_Ebs_396

Dear Author,

During the preparation of your manuscript for typesetting some questions have arisen. These are listed below. Please check your typeset proof carefully and mark any corrections in the margin of the proof or compile them as a separate list. This form should then be returned with your marked proof/list of corrections to John Wiley.

This form should then be returned with your marked proof/list of corrections to N.S. Pandian, Deputy Manager, Macmillan India Ltd., Book Division-IPD, Midford Crescent, New No. 159/1 (Old No. 53/1), Richmond Road, Bangalore-560025, India, Tel: +91-80-51237312; +91-80-51237313, Fax: +91-80-51237310, E-mail: ns.pandian@macmillan-india.co.in

Queries and/or remarks

AU:1	Is the expansion of DNA OK? Please clarify.
AU:2	Is the expansion of SNR OK?
AU:3	Please provide the citation for the reference 35 in the text.